MATCH
Communications in Mathematical and in Computer Chemistry

MATCH Commun. Math. Comput. Chem. **96** (2026) 99–128
ISSN: 0340–6253
doi: 10.46793/match.96-1.29925

Pattern Formation in an Enzyme-Catalyzed Reaction-Diffusion System on Complex Networks: The Coupling Mechanism of Topology and Dynamics

Jiaying Zhou[a], Xingzhuo Hua[a], Yu Chen[a], Yong Ye[b,*]

[a] *College of Science, Nanjing Forestry University, Nanjing, Jiangsu 210037, China*

[b] *School of Statistics and Data Science, Nanjing Audit University, Nanjing, Jiangsu 211815, China*

yong_ye1994@163.com

(Received November 18, 2025)

Abstract

This paper examines spatiotemporal dynamics in an enzyme-catalyzed reaction-diffusion system on complex networks. A generalized model with specific nonlinear reaction terms is developed. Analysis of the homogeneous system determines multiple equilibrium existence and stability, identifies bistability regions, and proves subcritical Hopf bifurcation occurrence. For network systems, conditions for Turing instability, Hopf bifurcation, and Turing-Hopf bifurcation are established using a theoretical framework incorporating network Laplacian eigenvalues. Numerical simulations demonstrate network average degree regulates pattern formation, with intermediate connectivity promoting spatiotemporal patterns while sparse or dense connectivity suppresses them. Identification of Turing-Hopf bifurcation points reveals interactions between temporal oscillations

*Corresponding author.

and spatial patterning. This work provides theoretical and numerical foundations for understanding network topology effects on biochemical pattern formation.

1 Introduction

Enzyme-catalyzed reaction systems serve as a fundamental paradigm for understanding nonlinear dynamics and pattern formation in biochemical processes. The pioneering work of [1] revealed that the interplay between reaction kinetics and diffusion can lead to spontaneous spatial pattern formation, a phenomenon now ubiquitously known as Turing patterns. Since then, reaction-diffusion systems have been extensively employed to model a wide array of spatiotemporal behaviors in chemical, biological, and ecological contexts [2–7].

In particular, enzyme-catalyzed systems exhibit a rich spectrum of dynamic phenomena, including multistability, periodic oscillations, and various spatial patterns. A generalized dimensionless form of such a system is often described by:

$$\begin{cases} \dfrac{\mathrm{d}u}{\mathrm{d}t} = \alpha - F_1(u,v) - F_3(u), \\ \dfrac{\mathrm{d}v}{\mathrm{d}t} = \beta\left(F_1(u,v) - F_2(v)\right), \end{cases} \tag{1}$$

where u and v represent the concentrations of the substrate and product, respectively. The nonlinear function $F_1(u,v)$ denotes the rate law, whose specific form critically influences the system's dynamics. System (1) kinetics are governed by the positive parameters α and β. Recent studies have explored various forms of $F_1(u,v)$. For instance, Su and Xu conducted a comprehensive bifurcation analysis of an enzyme-catalyzed reaction system with cubic rate law $F_1(u,v) = uv^2$, identifying saddle-node, Bogdanov-Takens, and Hopf bifurcations, and proving that the weak focus has order at most two [8]. Similarly, Wu and Yang performed a detailed bifurcation analysis of an enzyme-catalyzed reaction model with Langmuir-Hinshelwood mechanism, demonstrating the existence of saddle-node, Hopf, and Bogdanov-Takens bifurcations in the corresponding tem-

poral system [9].

Considering the concentration difference in different spatial locations, researchers have introduced diffusion terms into homogeneous systems to study the spatio-temporal dynamics. For example, Ko conducted a comprehensive study on the bifurcations and asymptotic behavior of positive steady-states in an enzyme-catalyzed reaction-diffusion system, revealing the global bifurcation structure and pattern formation mechanisms [10]. Atabaigi et al. performed a detailed bifurcation analysis of a reaction-diffusion enzyme-catalyzed system arising from glycolysis, investigating both spatially homogeneous and nonhomogeneous periodic solutions as well as nonconstant steady states under homogeneous Neumann boundary conditions [11]. Further extending this line of research, Chen and Li investigated a diffusive model with a cubic rate law $F_1(u, v) = uv^2$, establishing rigorous conditions for Turing instability and demonstrating the emergence of spot, stripe, and mixed patterns [12]. In a subsequent study, Zhao et al. examined a system with $F_1(u, v) = uv$, revealing the coexistence of temporal, spatial, and spatiotemporal oscillations induced by Hopf bifurcation, Turing instability, and Turing–Hopf bifurcation, respectively [13]. Furthermore, they also considered the case of $F_1(u, v) = uv^3$ [14].

Despite these advances, two significant aspects remain less explored. First, most existing models are confined to low-order polynomial kinetics, such as quadratic or cubic forms. The introduction of more complex nonlinearities may unveil novel bifurcation scenarios and pattern formation mechanisms due to stronger feedback effects. Second, the spatial domain in classical studies is typically assumed to be a continuous medium or a regular lattice. However, many real-world biochemical systems, including intracellular metabolic networks, biofilm communities, and distributed enzymatic reactors, are inherently structured as complex networks. The topology of such networks, for instance small-world or scale-free properties, can profoundly influence the propagation of chemical signals and the stability of dynamic states [15–18].

Motivated by the aforementioned insights and gaps in the literature, we propose a generalized enzyme-catalyzed reaction-diffusion model defined on a complex network. The model incorporates specific, mathematically

tractable nonlinear forms to serve as a minimal yet paradigmatic framework. In particular, the reaction terms are specified as $F_1(u,v) = uv$, $F_3(u) = \gamma u^2$, and $F_2(v) = \frac{v}{v+1}$. The latter follows the classic Michaelis-Menten form, describing a non-cooperative, saturable reaction rate. This represents a deliberate and simplified choice compared to more complex cooperative kinetics. Its purpose is to provide a well-established, analytically manageable foundation that allows us to isolate and systematically investigate the fundamental coupling between network topology and reaction-diffusion dynamics, without the additional algebraic complexity introduced by cooperative effects. The governing equations are thus:

$$\begin{cases} \dfrac{\partial u_i}{\partial t} = d_1 \sum_{j=1}^{N} L_{ij} u_j + \alpha - u_i v_i - \gamma u_i^2, \\ \dfrac{\partial v_i}{\partial t} = d_2 \sum_{j=1}^{N} L_{ij} v_j + \beta \left(u_i v_i - \dfrac{v_i}{v_i + 1} \right), \end{cases} \tag{2}$$

where $u_i(t)$ and $v_i(t)$ denote the concentrations of the substrate and product at the i-th node of the network, respectively. The matrix $L = (L_{ij})$ is the discrete Laplacian operator encoding the network's topology, defined as $L_{ij} = A_{ij} - k_i \delta_{ij}$, with A being the adjacency matrix, k_i the degree of node i, and δ_{ij} the Kronecker delta.

The structure of this paper is organized as follows. In Sec. 2, we determine the types, stability, and Hopf bifurcation of the homogeneous system. In Sec. 3, we explore the Turing instability, Hopf bifurcation, and Turing-Hopf bifurcation of the system on complex networks. Numerical results are presented throughout the theoretical analysis to verify the conclusions. Finally, we end this paper with a discussion in Sec. 4.

2 Dynamics analysis of homogeneous system

2.1 Homogeneous equilibria

For the homogeneous system without diffusion, we set $d_1 = d_2 = 0$ in equation (2), yielding the ordinary differential equations:

$$\begin{cases} \dfrac{\mathrm{d}u}{\mathrm{d}t} = \alpha - uv - \gamma u^2, \\ \dfrac{\mathrm{d}v}{\mathrm{d}t} = \beta \left(uv - \dfrac{v}{v+1} \right), \end{cases} \tag{3}$$

The equilibria (u_*, v_*) satisfy:

$$\alpha - u_* v_* - \gamma u_*^2 = 0, \tag{4}$$

$$u_* v_* - \frac{v_*}{v_* + 1} = 0. \tag{5}$$

From equation (5), we obtain:

$$v_* \left(u_* - \frac{1}{v_* + 1} \right) = 0. \tag{6}$$

For the boundary equilibrium case, when $v_* = 0$ is substituted into equation (4), we obtain $\alpha - \gamma u_*^2 = 0$, which yields $u_* = \sqrt{\frac{\alpha}{\gamma}}$, thus establishing the boundary equilibrium point $E_0 = (u_0, v_0) = \left(\sqrt{\frac{\alpha}{\gamma}}, 0 \right)$.

For the interior equilibria case where $u_* - \dfrac{1}{v_* + 1} = 0$ implies $u_* = \dfrac{1}{v_* + 1}$, substituting into equation (4):

$$\alpha - \left(\frac{1}{v_* + 1} \right) v_* - \gamma \left(\frac{1}{v_* + 1} \right)^2 = 0. \tag{7}$$

Multiplying through by $(v_* + 1)^2$:

$$\alpha (v_* + 1)^2 - v_* (v_* + 1) - \gamma = 0. \tag{8}$$

Expanding yields the quadratic equation:

$$(\alpha - 1)v_*^2 + (2\alpha - 1)v_* + (\alpha - \gamma) = 0. \tag{9}$$

A comprehensive analysis of this quadratic equation reveals that two distinct positive interior equilibrium points exist if and only if the following parameter conditions are satisfied:

$$\frac{1}{2} < \alpha < 1 \quad \text{and} \quad \gamma > \alpha. \tag{10}$$

Under these conditions, the two interior equilibria are given by:

$$v_1 = \frac{-(2\alpha - 1) - \sqrt{4\gamma(\alpha - 1) + 1}}{2(\alpha - 1)}, \quad u_1 = \frac{1}{v_1 + 1}, \tag{11}$$

$$v_2 = \frac{-(2\alpha - 1) + \sqrt{4\gamma(\alpha - 1) + 1}}{2(\alpha - 1)}, \quad u_2 = \frac{1}{v_2 + 1}, \tag{12}$$

with $v_1 > v_2 > 0$ and $u_1 < u_2$. The corresponding equilibrium points are denoted as $E_1 = (u_1, v_1)$ and $E_2 = (u_2, v_2)$. The coexistence of three equilibrium points (E_0, E_1, E_2) indicates the potential for bistability and complex switching phenomena in the system, which are fundamental for understanding pattern formation mechanisms in enzyme-catalyzed reaction systems.

Based on the theoretical analysis above, we validate the complex dynamical behaviors in the enzyme-catalyzed reaction system through numerical bifurcation diagrams. As shown in Figure 1, when the parameter α varies within specific ranges, the system exhibits rich nonlinear phenomena: the coexistence of three equilibrium points (the boundary equilibrium E_0 and two interior equilibria E_1 and E_2) confirms the equilibrium structure predicted theoretically; two saddle-node bifurcation points (SN_1 and SN_2) demarcate the existence region of bistability; and the emergence of a Hopf bifurcation point (H) indicates the potential for periodic oscillatory behavior in the system. These numerical results not only verify the correctness of the theoretical analysis but also reveal the complex stability transition mechanisms within the parameter space. To deeply understand

the mathematical essence of these dynamical phenomena, we proceed to conduct a detailed analysis of the system's local stability in the following subsection.

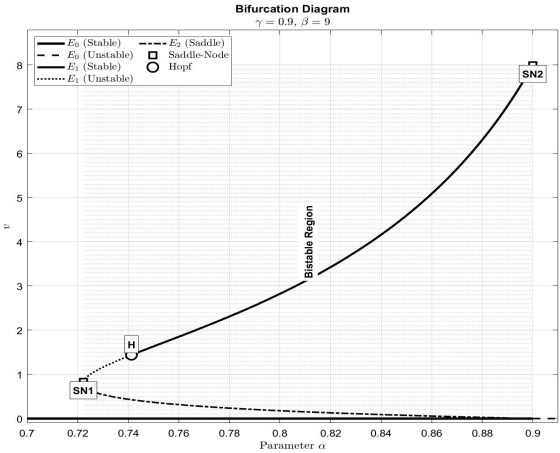

Figure 1. Bifurcation diagram showing the product concentration v as a function of the parameter α. The solid lines represent stable equilibria, dashed lines unstable equilibria, and dash-dotted lines saddle points. Saddle-node (SN) and Hopf (H) bifurcation points are marked. The bistable region is shaded. Parameters: $\gamma = 0.9$, $\beta = 9$.

2.2 Linear stability analysis

The local stability characteristics of each equilibrium point are determined by linearizing the system around the equilibrium. The Jacobian matrix evaluated at (u_*, v_*) is:

$$J = \begin{pmatrix} \dfrac{\partial f}{\partial u} & \dfrac{\partial f}{\partial v} \\ \dfrac{\partial g}{\partial u} & \dfrac{\partial g}{\partial v} \end{pmatrix}_{(u_*, v_*)}, \tag{13}$$

where $f(u,v) = \alpha - uv - \gamma u^2$ and $g(u,v) = \beta\left(uv - \frac{v}{v+1}\right)$. Computing the partial derivatives:

$$\frac{\partial f}{\partial u} = -v - 2\gamma u, \ \frac{\partial f}{\partial v} = -u, \ \frac{\partial g}{\partial u} = \beta v, \ \frac{\partial g}{\partial v} = \beta\left(u - \frac{1}{(v+1)^2}\right).$$

The characteristic equation is given by:

$$\lambda^2 - \mathrm{tr}(J)\lambda + \det(J) = 0, \tag{14}$$

where the trace and determinant are:

$$\mathrm{tr}(J) = J_{11} + J_{22} = -v_* - 2\gamma u_* + \beta\left(u_* - \frac{1}{(v_*+1)^2}\right), \tag{15}$$

$$\det(J) = J_{11}J_{22} - J_{12}J_{21}. \tag{16}$$

The stability criteria are:

- Stable node/focus: $\mathrm{tr}(J) < 0$ and $\det(J) > 0$;
- Unstable node/focus: $\mathrm{tr}(J) > 0$ and $\det(J) > 0$;
- Saddle point: $\det(J) < 0$.

For $E_0 = \left(\sqrt{\frac{\alpha}{\gamma}}, 0\right)$, the Jacobian matrix simplifies to:

$$J(E_0) = \begin{pmatrix} -2\sqrt{\alpha\gamma} & -\sqrt{\frac{\alpha}{\gamma}} \\ 0 & \beta\left(\sqrt{\frac{\alpha}{\gamma}} - 1\right) \end{pmatrix}. \tag{17}$$

The eigenvalues are $\lambda_1 = -2\sqrt{\alpha\gamma} < 0$ and $\lambda_2 = \beta\left(\sqrt{\frac{\alpha}{\gamma}} - 1\right)$. Thus, E_0 is stable when $\sqrt{\frac{\alpha}{\gamma}} < 1$ (i.e., $\gamma > \alpha$) and unstable otherwise.

For the interior equilibria E_1 and E_2, utilizing the relation $u_* = \frac{1}{v_*+1}$, the Jacobian matrix simplifies to:

$$J = \begin{pmatrix} J_{11} & J_{12} \\ J_{21} & J_{22} \end{pmatrix} = \begin{pmatrix} -v_* - \frac{2\gamma}{v_*+1} & -\frac{1}{v_*+1} \\ \beta v_* & \beta\frac{v_*}{(v_*+1)^2} \end{pmatrix}.$$

The determinant and trace are given by:

$$\det(J) = J_{11}J_{22} - J_{12}J_{21} = \beta v_* \frac{v_* + 1 - 2\gamma}{(v_* + 1)^3}, \tag{18}$$

$$\mathrm{tr}(J) = J_{11} + J_{22} = -v_* - \frac{2\gamma}{v_* + 1} + \beta \frac{v_*}{(v_* + 1)^2}. \tag{19}$$

Theorem 1. *Let E_1 and E_2 be the interior equilibria with $v_1 > v_2$, where v_1 and v_2 are the roots of:*

$$(\alpha - 1)v^2 + (2\alpha - 1)v + \alpha - \gamma = 0.$$

Then the stability properties are as follows:

- *For equilibrium E_2 (with smaller v_2): Since $v_2 + 1 - 2\gamma < 0$, we have $\det(J) < 0$. Therefore, E_2 is always a saddle point (unstable).*
- *For equilibrium E_1 (with larger v_1): Since $v_2 + 1 - 2\gamma > 0$, we have $\det(J) > 0$. Therefore, the stability of E_1 is determined by the trace, it is stable for $\beta < \beta_H$, undergoes a Hopf bifurcation at $\beta = \beta_H$, and unstable for $\beta > \beta_H$ with $\beta_H = (v_1 + 1)^2 + \frac{2\gamma(v_1+1)}{v_1}$.*

Proof. The stability properties of the interior equilibria E_1 and E_2 are determined through analysis of the Jacobian matrix eigenvalues.

For equilibrium E_2, the condition $v_2 + 1 - 2\gamma < 0$ implies $\det(J(E_2)) = \beta v_2 \frac{v_2+1-2\gamma}{(v_2+1)^3} < 0$, establishing E_2 as a saddle point with one positive and one negative eigenvalue.

For equilibrium E_1, the condition $v_1 + 1 - 2\gamma > 0$ ensures $\det(J(E_1)) > 0$. The stability is governed by the trace $\mathrm{tr}(J(E_1)) = -v_1 - \frac{2\gamma}{v_1+1} + \beta \frac{v_1}{(v_1+1)^2}$. Setting $\mathrm{tr}(J(E_1)) = 0$ yields the critical bifurcation parameter value:

$$\beta_H = (v_1 + 1)^2 + \frac{2\gamma(v_1 + 1)}{v_1},$$

where $v_1 = \frac{-(2\alpha-1)+\sqrt{(2\alpha-1)^2-4(\alpha-1)(\alpha-\gamma)}}{2(\alpha-1)}$. The transversality condition is verified by computing $\frac{\mathrm{d}}{\mathrm{d}\beta}\mathrm{tr}(J(E_1)) = \frac{v_1}{(v_1+1)^2} > 0$, confirming that the real parts of the complex conjugate eigenvalues cross the imaginary axis with non-zero speed. Consequently, the stability regions are characterized

as follows: E_1 is asymptotically stable for $0 < \beta < \beta_H$; A Hopf bifurcation occurs at $\beta = \beta_H$; E_1 is unstable for $\beta > \beta_H$. ■

Based on the theoretical stability analysis presented above, we conduct numerical simulations to validate the stability properties of the equilibrium points in the enzyme-catalyzed reaction system. Time series plots (Figure 2) and phase portraits (Fig. 3) are generated to illustrate the dynamic behavior of the system under different parameter regimes. The time series analysis clearly demonstrates the transition from stable convergence to equilibrium for $\beta = 8.5$, to sustained oscillatory behavior at the Hopf bifurcation point $\beta = 9$, and finally to unstable dynamics for $\beta = 9.5$. Correspondingly, the phase portrait at the bifurcation point demonstrates oscillatory behavior around equilibrium E_1, indicating the formation of limit cycles. These numerical observations are consistent with the theoretical framework of stability. The experiments provide evidence of dynamical transitions in the enzyme-catalyzed reaction system. To determine the stability of the oscillatory solutions and establish the bifurcation type, we proceed to analyze the Hopf bifurcation, which characterizes the conditions for stability loss and oscillation emergence.

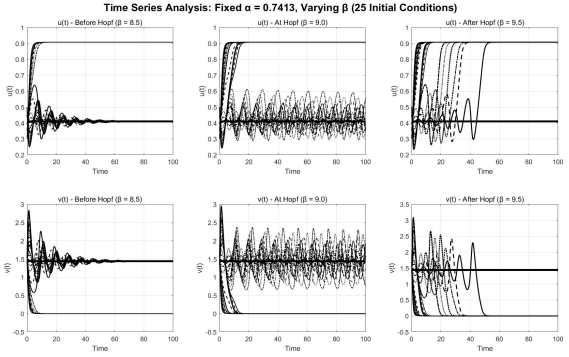

Figure 2. Time series of substrate (u) and product (v) concentrations for different values of β, with fixed $\alpha = 0.7413$. The system exhibits stable convergence to equilibrium for $\beta = 8.5$, sustained oscillations at the Hopf bifurcation point $\beta = 9$, and unstable behavior for $\beta = 9.5$.

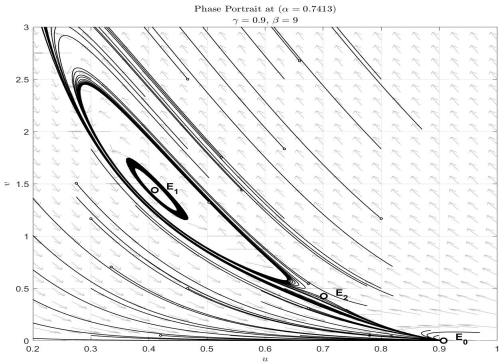

Figure 3. Phase portrait analysis at the Hopf bifurcation point ($\alpha = 0.7413$, $\beta = 9.0$, $\gamma = 0.9$). The plot illustrates the vector field (light gray arrows) and multiple trajectories (black lines with varying styles) from different initial conditions. Three equilibrium points are identified: the boundary equilibrium E_0 (stable node) and interior equilibria E_1 (center with unstable limit cycle) and E_2 (saddle point).

2.3 Hopf bifurcation analysis

Based on the previous linear stability analysis, the system may undergo a Hopf bifurcation at the interior equilibrium point $E_1 = (u_1, v_1)$, where v_1 is the larger positive root, under the parameter conditions $\frac{1}{2} < \alpha < 1$ and $\gamma > \alpha$. We now analyze the existence of Hopf bifurcation using β as the bifurcation parameter.

Theorem 2. *(i) System* (3) *undergoes a Hopf bifurcation at the equilibrium point E_1 when the following conditions are satisfied:*

$$\mathrm{tr}(J) = 0, \quad \det(J) > 0, \quad \frac{\mathrm{d}}{\mathrm{d}\beta}\mathrm{tr}(J)\bigg|_{\beta=\beta_H} > 0,$$

where the critical value β_H is given by:

$$\beta_H = (v_1 + 1)^2 + \frac{2\gamma(v_1 + 1)}{v_1},$$

and v_1 is determined by:

$$v_1 = \frac{-(2\alpha-1) - \sqrt{4\gamma(\alpha-1)+1}}{2(\alpha-1)}.$$

(ii) If the Lyapunov coefficient $l_1 < 0$, then the Hopf bifurcation is supercritical and the bifurcating periodic solution is stable; if $l_1 > 0$, then the Hopf bifurcation is subcritical and the bifurcating periodic solution is unstable.

Proof. First, we prove that system (3) undergoes a Hopf bifurcation at $\beta = \beta_H$. The Jacobian matrix at the equilibrium point E_1 is:

$$J = \begin{pmatrix} f_u & f_v \\ g_u & g_v \end{pmatrix}_{(u_1,v_1)},$$

where $f(u,v) = \alpha - uv - \gamma u^2$ and $g(u,v) = \beta\left(uv - \frac{v}{v+1}\right)$. At E_1, we have $u_1 = \frac{1}{v_1+1}$, and v_1 satisfies:

$$v_1 = \frac{-(2\alpha-1) - \sqrt{4\gamma(\alpha-1)+1}}{2(\alpha-1)}.$$

Computing the partial derivatives:

$$f_u = -v - 2\gamma u,\ f_v = -u,\ g_u = \beta v,\ g_v = \beta u - \beta\frac{1}{(v+1)^2}.$$

At E_1:

$$a_{10} = -v_1 - 2\gamma u_1,\ a_{01} = -\frac{1}{v_1+1},\ b_{10} = \beta v_1,\ b_{01} = \beta\frac{v_1}{(v_1+1)^2}.$$

The trace and determinant are:

$$\operatorname{tr}(J) = a_{10} + b_{01} = -v_1 - 2\gamma u_1 + \beta\frac{v_1}{(v_1+1)^2},$$
$$\det(J) = a_{10}b_{01} - a_{01}b_{10} = \beta v_1\frac{v_1+1-2\gamma}{(v_1+1)^3}.$$

When $\beta = \beta_H$, we have $\operatorname{tr}(J) = 0$, and from stability analysis we know

$\det(J) > 0$. The eigenvalues are $\lambda = \pm i\sqrt{\det(J)}$. Let $\lambda = \eta(\beta) \pm \omega(\beta)i$ be the roots of the characteristic equation $\lambda^2 - \mathrm{tr}(J)\lambda + \det(J) = 0$, then:

$$\eta(\beta) = \frac{\mathrm{tr}(J)}{2},\ \omega(\beta) = \frac{\sqrt{4\det(J) - (\mathrm{tr}(J))^2}}{2},\ \left.\frac{\mathrm{d}\eta(\beta)}{\mathrm{d}\beta}\right|_{\beta=\beta_H} = \frac{1}{2}\frac{v_1}{(v_1+1)^2}.$$

The transversality condition is satisfied, therefore system (3) undergoes a Hopf bifurcation at $\beta = \beta_H$.

To determine the direction and stability of the bifurcation, we compute the first Lyapunov coefficient l_1. Let $u = u_1 + x$ and $v = v_1 + y$, shifting the equilibrium to the origin. The system becomes:

$$\frac{\mathrm{d}x}{\mathrm{d}t} = a_{10}x + a_{01}y + F(x,y),\ \frac{\mathrm{d}y}{\mathrm{d}t} = b_{10}x + b_{01}y + G(x,y),$$

where $F(x,y)$ and $G(x,y)$ are the higher-order terms:

$$\begin{aligned} F(x,y) =& a_{20}x^2 + a_{11}xy + a_{02}y^2 \\ &+ a_{30}x^3 + a_{21}x^2y + a_{12}xy^2 + a_{03}y^3 + \cdots, \\ G(x,y) =& b_{20}x^2 + b_{11}xy + b_{02}y^2 \\ &+ b_{30}x^3 + b_{21}x^2y + b_{12}xy^2 + b_{03}y^3 + \cdots. \end{aligned}$$

Computing the coefficients:

$$\begin{aligned} &a_{20} = -\gamma,\ a_{11} = -1,\ a_{02} = a_{30} = a_{21} = a_{12} = a_{03} = 0, \\ &b_{11} = \beta,\ b_{02} = \frac{\beta}{(v_1+1)^3},\ b_{20} = b_{30} = b_{21} = b_{12} = 0,\ b_{03} = -\frac{\beta}{(v_1+1)^4}. \end{aligned}$$

At $\beta = \beta_H$, we have $b_{01} = -a_{10}$. The Lyapunov coefficient l_1 is given by:

$$\begin{aligned} l_1 = \frac{-3\pi}{2a_{01}\Delta^{3/2}} \Bigg[& a_{10}b_{01}(a_{11}^2 + a_{11}b_{02} + a_{02}b_{11}) \\ & + a_{10}a_{01}(b_{11}^2 + b_{11}a_{02} + b_{02}a_{11}) + b_{10}^2(a_{11}a_{02} + 2a_{02}b_{02}) \\ & - 2a_{10}b_{10}(b_{02}^2 - a_{20}a_{02}) - 2a_{10}a_{01}(a_{20}^2 - b_{20}b_{02}) \\ & - a_{01}^2(2a_{20}b_{20} + b_{11}b_{20}) + (a_{01}b_{10} - 2a_{10}^2)(b_{11}b_{02} - a_{11}a_{20}) \\ & - (a_{10}^2 + a_{01}b_{10})\big(3(b_{10}b_{03} - a_{01}a_{30}) + 2a_{10}(a_{21} + b_{12}) \\ & + (b_{10}a_{12} - a_{01}b_{21})\big) \Bigg], \end{aligned} \tag{20}$$

where $\Delta = \beta v_1 \frac{v_1+1-2\gamma}{(v_1+1)^3}$. Substituting the coefficients and simplifying (noting that $a_{02} = 0$, $a_{20} = -\gamma$, $a_{11} = -1$, $b_{11} = \beta$, $b_{02} = \beta/(v_1+1)^3$, $b_{20} = 0$, $a_{30} = 0$, $a_{21} = 0$, $b_{12} = 0$, $a_{12} = 0$, $b_{21} = 0$, $b_{03} = -\beta/(v_1+1)^4$), we obtain:

$$\begin{aligned} l_1 = \frac{-3\pi}{2a_{01}\Delta^{3/2}} \big[& a_{10}b_{01}(1 - b_{02}) + a_{10}a_{01}(\beta^2 - \beta b_{02}) - 2a_{10}b_{10}b_{02}^2 \\ & -2a_{10}a_{01}\gamma^2 + (a_{01}b_{10} - 2a_{10}^2)(\beta b_{02} - \gamma) - 3b_{10}b_{03}(a_{10}^2 + a_{01}b_{10}) \big]. \end{aligned}$$

If $l_1 < 0$, the Hopf bifurcation is supercritical and the bifurcating periodic solution is stable; if $l_1 > 0$, the Hopf bifurcation is subcritical and the bifurcating periodic solution is unstable. ■

Based on the Hopf bifurcation analysis, we provide numerical verification to illustrate the subcritical Hopf bifurcation for the parameters $\alpha = 0.7413$, $\beta = 9.0$, and $\gamma = 0.9$. The interior equilibrium point is computed as $E_1 = (u_1, v_1) = (0.4100, 1.4393)$, where v_1 is determined by the formula $v_1 = \frac{-(2\alpha-1)-\sqrt{4\gamma(\alpha-1)+1}}{2(\alpha-1)}$. At this equilibrium, the trace of the Jacobian matrix vanishes, $\mathrm{tr}(J) = 0$, while the determinant remains positive, $\det(J) > 0$, satisfying the conditions for a Hopf bifurcation. The critical bifurcation parameter is calculated as $\beta_H = (v_1+1)^2 + \frac{2\gamma(v_1+1)}{v_1} \approx 9.007$, which is close to the chosen $\beta = 9.0$, indicating the system is near the bifurcation point. The first Lyapunov coefficient is computed as $l_1 = 408.590568 > 0$. According to Theorem 2, since $l_1 > 0$, the Hopf bifur-

cation is subcritical. This implies that the bifurcating periodic solutions are unstable and exist for parameter values $\beta < \beta_H$, leading to potentially abrupt transitions in system dynamics.

Figure 4 shows the bifurcation diagrams with respect to parameters α and β. The diagrams clearly demonstrate the onset of oscillations as the parameters cross critical values. Figure 5 provides direct evi-

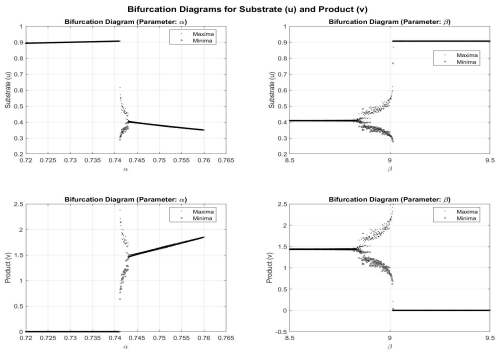

Figure 4. Bifurcation diagrams showing the dependence on parameters α and β. The black dots represent maxima and white circles represent minima of the oscillations.

dence of the subcritical nature through the phase portrait analysis. Two trajectories with closely spaced initial conditions $(0.503485, 1.32198)$ and $(0.503485, 1.31198)$ exhibit dramatically different behaviors: the trajectory starting inside the unstable limit cycle (black) converges to the equilibrium E_1, while the trajectory starting outside (gray) diverges away from the equilibrium. This behavior characterizes the unstable nature of the limit cycle generated by the subcritical Hopf bifurcation.The positive Lyapunov coefficient confirms the destabilizing effect of the nonlinear terms, resulting in a subcritical bifurcation where small perturbations can cause significant changes in system behavior near the equilibrium E_1. This numerical verification aligns perfectly with the theoretical analysis presented in Theorem 2.

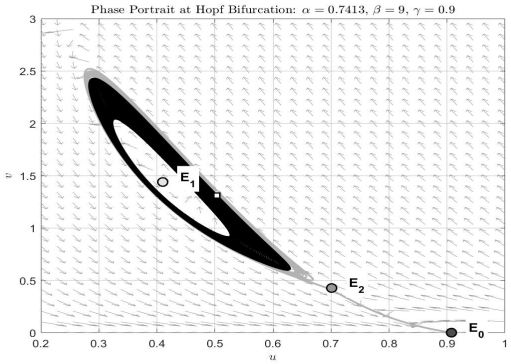

Figure 5. Phase portrait near the Hopf bifurcation point. The black trajectory starts inside the unstable limit cycle and converges to E_1, while the gray trajectory starts outside and diverges, demonstrating the instability of the limit cycle.

3 Spatiotemporal dynamic analysis on networks

3.1 Turing instability analysis on networks

For the network-based system described by equation (2), we analyze Turing instability around the homogeneous equilibrium $E_1 = (u_1, v_1)$ [19]. Consider small perturbations δu_i and δv_i around the equilibrium:

$$u_i = u_1 + \delta u_i, \quad v_i = v_1 + \delta v_i. \tag{21}$$

The linearized dynamics are governed by:

$$\begin{cases} \dfrac{\partial \delta u_i}{\partial t} = d_1 \sum_{j=1}^{N} L_{ij} \delta u_j + a_{10} \delta u_i + a_{01} \delta v_i, \\ \dfrac{\partial \delta v_i}{\partial t} = d_2 \sum_{j=1}^{N} L_{ij} \delta v_j + b_{10} \delta u_i + b_{01} \delta v_i. \end{cases} \tag{22}$$

Expanding the perturbations in terms of the Laplacian eigenvectors $\{\phi^{(\alpha)}\}$:

$$\delta u_i(t) = \sum_{\alpha=1}^{N} W_\alpha^1 e^{\lambda_\alpha t} \phi_i^{(\alpha)}, \quad \delta v_i(t) = \sum_{\alpha=1}^{N} W_\alpha^2 e^{\lambda_\alpha t} \phi_i^{(\alpha)}, \tag{23}$$

and utilizing the eigenvalue equation $\sum_{j=1}^{N} L_{ij}\phi_j^{(\alpha)} = \Lambda_\alpha \phi_i^{(\alpha)}$, we obtain the characteristic equation for each mode α:

$$\lambda_\alpha \begin{pmatrix} W_\alpha^1 \\ W_\alpha^2 \end{pmatrix} = \begin{pmatrix} a_{10} + d_1\Lambda_\alpha & a_{01} \\ b_{10} & b_{01} + d_2\Lambda_\alpha \end{pmatrix} \begin{pmatrix} W_\alpha^1 \\ W_\alpha^2 \end{pmatrix}. \tag{24}$$

The characteristic polynomial becomes:

$$\lambda_\alpha^2 - \mathrm{tr}(J_\alpha)\lambda_\alpha + \det(J_\alpha) = 0, \tag{25}$$

where

$$\begin{aligned} \mathrm{tr}(J_\alpha) &= a_{10} + b_{01} + (d_1 + d_2)\Lambda_\alpha, \\ \det(J_\alpha) &= a_{10}b_{01} - a_{01}b_{10} + (a_{10}d_2 + b_{01}d_1)\Lambda_\alpha + d_1 d_2 \Lambda_\alpha^2. \end{aligned}$$

Theorem 3. *Turing instability occurs at equilibrium E_1 when the following conditions are satisfied:*

- *The homogeneous system is stable: $a_{10}+b_{01} < 0$ and $a_{10}b_{01}-a_{01}b_{10} > 0$;*
- *There exists at least one Laplacian eigenvalue $\Lambda_\alpha < 0$ such that $\det(J_\alpha) < 0$;*
- *The diffusion coefficients satisfy the instability condition:*

$$a_{10}d_2 + b_{01}d_1 > 2\sqrt{d_1 d_2 (a_{10}b_{01} - a_{01}b_{10})}. \tag{26}$$

Proof. The first condition ensures stability of the homogeneous equilibrium E_1 without diffusion. For Turing instability to occur, diffusion must destabilize the system, which requires $\det(J_\alpha) < 0$ for some $\Lambda_\alpha < 0$. The minimum of $\det(J_\alpha)$ as a function of Λ_α occurs at:

$$\bar{\Lambda}_\alpha = -\frac{a_{10}d_2 + b_{01}d_1}{2d_1 d_2}, \tag{27}$$

with minimal value:

$$\det(J_\alpha)_{\min} = (a_{10}b_{01} - a_{01}b_{10}) - \frac{(a_{10}d_2 + b_{01}d_1)^2}{4d_1d_2}. \tag{28}$$

Turing instability requires $\det(J_\alpha)_{\min} < 0$, which yields condition (26). The instability occurs for Laplacian eigenvalues in the interval $\Lambda_\alpha^{(1)} < \Lambda_\alpha < \Lambda_\alpha^{(2)}$, where:

$$\Lambda_\alpha^{(1)} = \frac{-(a_{10}d_2 + b_{01}d_1) - \sqrt{\Delta}}{2d_1d_2},$$
$$\Lambda_\alpha^{(2)} = \frac{-(a_{10}d_2 + b_{01}d_1) + \sqrt{\Delta}}{2d_1d_2},$$

with $\Delta = (a_{10}d_2 + b_{01}d_1)^2 - 4d_1d_2(a_{10}b_{01} - a_{01}b_{10}) > 0$. ■

Remark. The critical value β_T for Turing bifurcation can be determined by setting $\det(J_\alpha)_{\min} = 0$:

$$(a_{10}b_{01} - a_{01}b_{10}) - \frac{(a_{10}d_2 + b_{01}d_1)^2}{4d_1d_2} = 0. \tag{29}$$

And obtain:

$$\beta v_1 \frac{v_1 + 1 - 2\gamma}{(v_1+1)^3} - \frac{\left[(-v_1 - \frac{2\gamma}{v_1+1})d_2 + \beta\frac{v_1}{(v_1+1)^2}d_1\right]^2}{4d_1d_2} = 0. \tag{30}$$

Solving for β, the critical Turing bifurcation parameter β_T satisfies:

$$\beta_T v_1 \frac{v_1 + 1 - 2\gamma}{(v_1+1)^3} = \frac{\left[\beta_T\frac{v_1d_1}{(v_1+1)^2} - d_2(v_1 + \frac{2\gamma}{v_1+1})\right]^2}{4d_1d_2}. \tag{31}$$

This yields a quadratic equation in β_T:

$$\left(\frac{v_1^2d_1^2}{4d_1d_2(v_1+1)^4}\right)\beta_T^2 - \left[\frac{v_1d_1d_2(v_1 + \frac{2\gamma}{v_1+1})}{2d_1d_2(v_1+1)^2} + \frac{v_1(v_1+1-2\gamma)}{(v_1+1)^3}\right]\beta_T + \frac{d_2^2(v_1 + \frac{2\gamma}{v_1+1})^2}{4d_1d_2} = 0. \tag{32}$$

Simplifying the coefficients:

$$A\beta_T^2 + B\beta_T + C = 0, \tag{33}$$

where

$$A = \frac{v_1^2 d_1}{4d_2(v_1+1)^4},\ B = -\frac{v_1(v_1^2+3v_1+2-2\gamma)}{2(v_1+1)^3},\ C = \frac{d_2(v_1^2+v_1+2\gamma)^2}{4d_1(v_1+1)^2}.$$

The physically relevant solution is:

$$\beta_T = \frac{-B \pm \sqrt{B^2-4AC}}{2A}, \tag{34}$$

where we take the negative branch to ensure $\beta_T > 0$ and $\beta_T < \beta_H$ for typical parameter values.

To validate the theoretical analysis and investigate the influence of network average degree on Turing pattern formation, we conducted systematic numerical experiments. The parameter settings were chosen as: $d_1 = 2$, $d_2 = 0.5$, $\alpha = 0.7413$, $\beta = 8.5$, $\gamma = 0.9$, which satisfy the Turing instability conditions. The calculated equilibrium point is $E_1 = (u_1, v_1) = (0.4100, 1.4393)$, with the Turing instability interval spanning from $\Lambda_\alpha^{(1)} = -2.8334$ to $\Lambda_\alpha^{(2)} = -0.1902$.

Figure 6 illustrates the dispersion relations and spatiotemporal evolution of Turing patterns in both ER random networks [20] and BA scale-free networks [21]. These two network types were chosen as classical prototypes: ER networks, characterized by random and homogeneous connectivity with a Poisson-like degree distribution, allow us to study dynamics in structurally unbiased settings; BA networks, featuring a power-law degree distribution with influential hubs, enable the investigation of how topological heterogeneity, specifically the pronounced disparity in node connectivity, affects pattern formation. A comparative analysis of these distinct topologies helps reveal the coupling mechanism between network architecture (randomness versus heterogeneity) and dynamical behaviors.

The dispersion relations (first column) demonstrate how the average degree $\langle k \rangle$, a fundamental parameter quantifying network connection den-

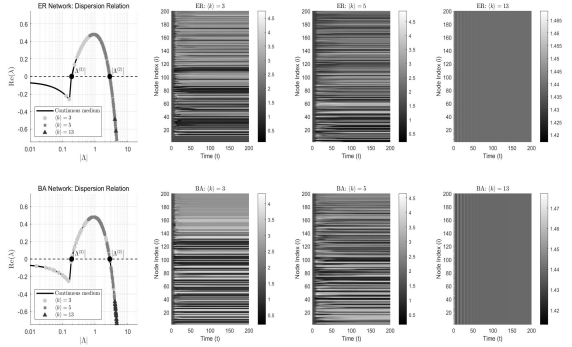

Figure 6. Influence of network average degree on Turing pattern. The first column shows dispersion relations, displaying growth rates corresponding to network eigenvalues under different average degrees; the right three columns show Turing patterns under corresponding average degrees, illustrating the spatiotemporal evolution of product concentration v. The top row represents ER random networks, while the bottom row represents BA scale-free networks.

sity, shapes the system's dynamics by altering the spectrum of Laplacian eigenvalues Λ_α. As $\langle k \rangle$ increases, the distribution of Λ_α changes significantly, leading to a non-monotonic trend in the growth rates $\mathrm{Re}(\lambda_\alpha)$ of Turing unstable modes: initially rising, then falling, and eventually exiting the Turing instability region. Specifically, when $\langle k \rangle$ increases from 3 to 13, the eigenvalue distribution becomes more concentrated and gradually shifts outside the Turing instability interval $(\Lambda^{(1)}, \Lambda^{(2)})$, thereby suppressing the formation of distinct Turing patterns. This result underscores how enhanced connectivity, modulated by $\langle k \rangle$, can stabilize the system and inhibit pattern-forming instabilities.

Turing patterns (right three columns) visually demonstrate this evolutionary process. Under low average degree conditions ($\langle k \rangle = 3$), both network types exhibit spatiotemporal oscillatory patterns while still maintaining homogeneous distributions in some local nodes. As the average degree increases to $\langle k \rangle = 5$, the network eigenvalues become uniformly distributed within the required range for Turing instability, meaning spatial heterogeneity is enhanced, and both network types display clear spatiotemporal

oscillatory patterns. However, when the average degree further increases to $\langle k \rangle = 13$, Turing patterns almost completely disappear, and the system approaches a homogeneous steady state. The theoretical mechanism behind this phenomenon lies in the enhanced diffusion coupling strength with increasing network average degree, allowing local perturbations to propagate and dissipate more rapidly throughout the network.

3.2 Hopf bifurcation analysis on networks

For the network-based system described by equation (2), Hopf bifurcation occurs at the homogeneous equilibrium $E_1 = (u_1, v_1)$ when eigenvalues cross the imaginary axis for some network mode.

Theorem 4. *The network system undergoes a Hopf bifurcation at equilibrium E_1 when there exists a Laplacian eigenvalue Λ_α satisfying the following conditions:*

- $\mathrm{tr}(J_\alpha) = a_{10} + b_{01} + (d_1 + d_2)\Lambda_\alpha = 0$*;*
- $\det(J_\alpha) > 0$*;*
- *Transversality condition:* $\left.\dfrac{\mathrm{d}}{\mathrm{d}\beta}\,\mathrm{tr}(J_\alpha)\right|_{\beta=\beta_H(\Lambda_\alpha)} \neq 0,$

where the critical parameter $\beta_H(\Lambda_\alpha)$ is given by:

$$\beta_H(\Lambda_\alpha) = \frac{v_1 + 2\gamma u_1 - (d_1 + d_2)\Lambda_\alpha}{u_1 - \frac{1}{(v_1+1)^2}}. \tag{35}$$

Proof. For each mode α, the characteristic equation $\lambda_\alpha^2 - \mathrm{tr}(J_\alpha)\lambda_\alpha + \det(J_\alpha) = 0$ has roots:

$$\lambda_\alpha = \frac{\mathrm{tr}(J_\alpha) \pm \sqrt{\mathrm{tr}(J_\alpha)^2 - 4\det(J_\alpha)}}{2}. \tag{36}$$

When $\mathrm{tr}(J_\alpha) = 0$ and $\det(J_\alpha) > 0$, the eigenvalues are purely imaginary:

$$\lambda_\alpha = \pm i\sqrt{\det(J_\alpha)}. \tag{37}$$

Setting $\mathrm{tr}(J_\alpha) = 0$ and substituting the Jacobian matrix elements:

$$-v_1 - 2\gamma u_1 + \beta\left(u_1 - \frac{1}{(v_1+1)^2}\right) + (d_1+d_2)\Lambda_\alpha = 0. \tag{38}$$

Solving for β yields the critical value:

$$\beta_H(\Lambda_\alpha) = \frac{v_1 + 2\gamma u_1 - (d_1+d_2)\Lambda_\alpha}{u_1 - \frac{1}{(v_1+1)^2}}. \tag{39}$$

Verifying the transversality condition:

$$\frac{\mathrm{d}}{\mathrm{d}\beta}\,\mathrm{tr}(J_\alpha) = u_1 - \frac{1}{(v_1+1)^2} > 0. \tag{40}$$

Since $u_1 = \frac{1}{v_1+1}$, this derivative is always positive, satisfying the transversality condition. ■

Remark. Specifically, for the homogeneous mode ($\Lambda_\alpha = 0$), the Hopf bifurcation critical parameter is:

$$\beta_H(0) = \frac{v_1 + 2\gamma u_1}{u_1 - \frac{1}{(v_1+1)^2}} = (v_1+1)^2 + \frac{2\gamma(v_1+1)}{v_1} = \beta_H. \tag{41}$$

This coincides with the Hopf bifurcation critical value for the continuous system.

To validate the theoretical analysis and investigate the influence of network average degree on Hopf bifurcation-induced spatiotemporal pattern formation, we conducted systematic numerical experiments. The parameter settings were chosen as: $d_1 = 0.02$, $d_2 = 0.01$, $\alpha = 0.7413$, $\gamma = 0.9$, which satisfy the Hopf bifurcation conditions. The calculated equilibrium point is $E_1 = (u_1, v_1) = (0.4100, 1.4393)$.

Figure 7 illustrates the Hopf bifurcation critical parameter relationships and corresponding spatiotemporal pattern evolution in both ER random networks and BA scale-free networks. The Hopf bifurcation diagrams (first column) reveal the variation of critical parameter $\beta_H(\Lambda_\alpha)$ with respect to network Laplacian eigenvalues Λ_α, where markers of different gray shades represent critical parameters corresponding to network eigenvalues

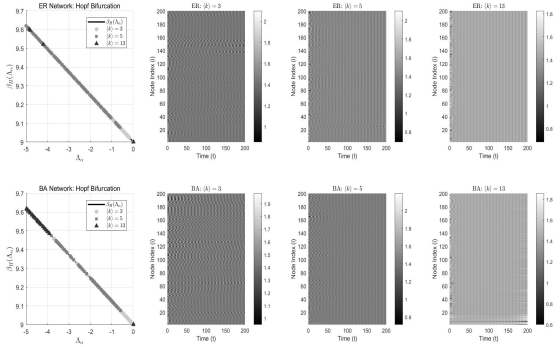

Figure 7. Influence of network average degree on Hopf bifurcation-induced spatiotemporal pattern. The first column shows Hopf bifurcation critical parameter β_H as a function of network eigenvalues Λ_α; the right three columns display spatiotemporal patterns under corresponding average degrees, illustrating the spatiotemporal evolution of product concentration v. The top row represents ER random networks, while the bottom row represents BA scale-free networks.

under different average degrees. The spatiotemporal patterns (right three columns) visually demonstrate this evolutionary process. Under low average degree conditions ($\langle k \rangle = 3$), both network types exhibit pronounced spatiotemporal oscillatory patterns with significant heterogeneity among nodes. However, when the average degree increases to $\langle k \rangle = 5$, the distribution of network eigenvalues makes it more difficult for the system to satisfy the Hopf bifurcation conditions, resulting in weakened spatiotemporal oscillatory patterns. When the average degree further increases to $\langle k \rangle = 13$, the spatiotemporal patterns almost completely disappear, and the system approaches a homogeneous steady state.

The theoretical mechanism underlying this phenomenon lies in the fact that as network average degree increases, the critical parameter $\beta_H(\Lambda_\alpha)$ for Hopf bifurcation occurrence requires higher thresholds. In our experiments, we selected $\beta = 9.0096$ slightly above the critical value for each network configuration. However, with increasing average degree, the enhanced network connectivity density strengthens diffusion coupling effects, allowing local perturbations to propagate and dissipate more rapidly

throughout the network, consequently suppressing the formation of Hopf bifurcation-induced spatiotemporal oscillatory patterns.

3.3 Turing-Hopf bifurcation analysis on networks

Turing-Hopf bifurcation occurs in parameter space where the Turing bifurcation curve and Hopf bifurcation curve intersect, indicating simultaneous loss of temporal and spatial stability.

Theorem 5. *The Turing-Hopf bifurcation point* $(\beta_{TH}, d_{1,TH})$ *satisfies the following conditions:*

- *There exists at least one mode* α *satisfying Hopf bifurcation condition:* $\mathrm{tr}(J_\alpha) = 0$ *and* $\det(J_\alpha) > 0$*;*
- *There exists at least one mode* $\kappa \neq \alpha$ *satisfying Turing bifurcation condition:* $\det(J_\kappa) = 0$*;*
- *Both bifurcations occur at the same parameter point.*

The following system of equations determines the Turing-Hopf bifurcation point:

$$\begin{aligned} &\beta_{TH} = \beta_H(\Lambda_\alpha) = \beta_T(\Lambda_\kappa),\ a_{10} + b_{01} + (d_1 + d_2)\Lambda_\alpha = 0, \\ &(a_{10}b_{01} - a_{01}b_{10}) - \frac{(a_{10}d_2 + b_{01}d_1)^2}{4d_1d_2} = 0, \end{aligned}$$

where the Jacobian matrix elements are evaluated at $(\beta_{TH}, d_{1,TH})$*.*

Proof. At the Turing-Hopf bifurcation point, the system simultaneously satisfies:

- For some mode α: $\mathrm{tr}(J_\alpha) = 0$, corresponding to Hopf bifurcation,
- For some mode κ: $\det(J_\kappa)_{\min} = 0$, corresponding to Turing bifurcation.

Expanding the Hopf bifurcation condition $\mathrm{tr}(J_\alpha) = 0$:

$$-v_1 - 2\gamma u_1 + \beta\left(u_1 - \frac{1}{(v_1+1)^2}\right) + (d_1 + d_2)\Lambda_\alpha = 0. \tag{42}$$

Expanding the Turing bifurcation condition $\det(J_\kappa)_{\min} = 0$:

$$\beta v_1 \frac{v_1 + 1 - 2\gamma}{(v_1+1)^3} - \frac{\left[\beta \frac{v_1 d_1}{(v_1+1)^2} - d_2\left(v_1 + \frac{2\gamma}{v_1+1}\right)\right]^2}{4 d_1 d_2} = 0. \tag{43}$$

These two equations together determine the position of the Turing-Hopf bifurcation point in the parameter space (β, d_1). ■

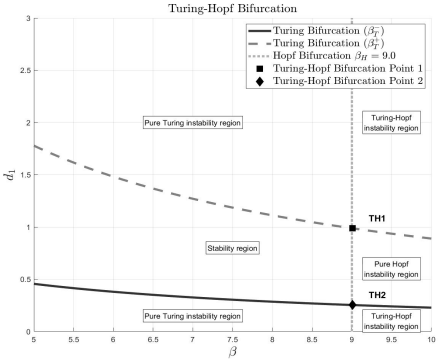

Figure 8. Turing-Hopf bifurcation diagram showing the interaction between Turing bifurcation curves (β_T^- and β_T^+) and Hopf bifurcation line ($\beta_H = 9.0006$). Two distinct Turing-Hopf bifurcation points (TH1 and TH2) are identified at ($\beta = 9.0096, d_1 = 0.9876$) and ($\beta = 9.0096, d_1 = 0.2532$), respectively. The diagram partitions the parameter space into distinct stability regions: pure Turing instability, pure Hopf instability, Turing-Hopf instability, and stable regions.

Figure 8 validates the existence conditions and characteristics of Turing-Hopf bifurcation in network systems. According to Theorem 5, Turing-Hopf bifurcation occurs at the intersection points of Turing bifurcation curves and Hopf bifurcation curves, indicating simultaneous loss of temporal and spatial stability in the system. The numerically computed Hopf bifurcation critical value is $\beta_H = 9.0006$, with the equilibrium point at $(u_1, v_1) = (0.4100, 1.4393)$, establishing parameter benchmarks for theoretical analysis. Two distinct Turing-Hopf bifurcation points are identified in the parameter space: TH1 located at ($\beta = 9.0096, d_1 = 0.9876$) and TH2 at ($\beta = 9.0096, d_1 = 0.2532$). These bifurcation points satisfy

the conditions specified in the theorem: under identical β parameters, the system simultaneously meets both the Hopf bifurcation condition (zero real part of eigenvalues) and the Turing bifurcation condition (zero characteristic determinant). The existence of these bifurcation points confirms the theoretical conclusion that Turing-Hopf bifurcation points are jointly determined by the Hopf bifurcation condition $\mathrm{tr}(J_\alpha) = 0$ and the Turing bifurcation condition $\det(J_\kappa)_{\min} = 0$.

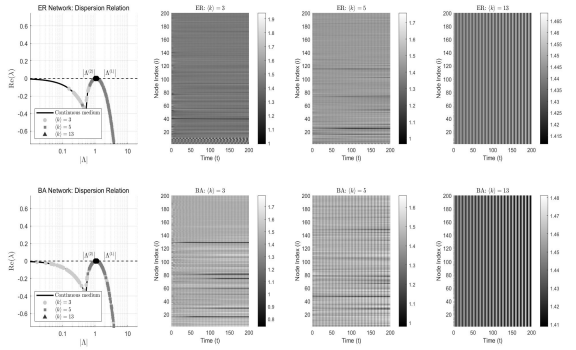

Figure 9. Dispersion relations and spatiotemporal patterns at Turing-Hopf bifurcation point. The first column shows dispersion relations, displaying growth rates corresponding to network eigenvalues under different average degrees. The right three columns illustrate spatiotemporal evolution of product concentration v under corresponding average degrees. The top row represents ER random networks, while the bottom row represents BA scale-free networks.

Guided by the parameter values determined from the Turing-Hopf bifurcation analysis, we conducted systematic numerical experiments to investigate pattern formation dynamics. The parameter configuration was selected at the first Turing-Hopf bifurcation point: $d_1 = 0.9876$, $d_2 = 0.5$, $\alpha = 0.7413$, $\beta = 9.0096$, $\gamma = 0.9$, with the corresponding equilibrium point $(u_1, v_1) = (0.4100, 1.4393)$. The Turing instability interval was computed as $\Lambda^{(1)} = -1.136431$ to $\Lambda^{(2)} = -1.017771$. Figure 9 presents the comprehensive numerical results, displaying dispersion relations and corresponding spatiotemporal patterns for both ER random networks and BA scale-free networks across different average degrees ($\langle k \rangle = 3, 5, 13$). The

selected parameters situate the system within the Turing-Hopf instability region, characterized by the simultaneous emergence of Turing patterns and Hopf bifurcation-induced spatiotemporal oscillations, as evidenced in the right subplots.

The dispersion relations (first column) demonstrate that under low average degree conditions ($\langle k \rangle = 3, 5$), the network eigenvalues are distributed within the Turing instability interval $(\Lambda^{(1)}, \Lambda^{(2)})$, enabling the formation of both spatial patterns and temporal oscillations. However, when the average degree increases to $\langle k \rangle = 13$, the network eigenvalue distribution shifts outside the Turing instability region, resulting in the disappearance of Turing patterns while maintaining the temporal periodic oscillations. These results indicate that network average degree serves as a crucial control parameter for regulating the formation of Turing patterns and spatiotemporal patterns, without fundamentally altering the inherent temporal oscillatory behavior.

4 Conclusion

In this paper, we have conducted a comprehensive investigation of the spatiotemporal dynamics in an enzyme-catalyzed reaction-diffusion system defined on complex networks. Our study reveals several key findings that advance the understanding of pattern formation mechanisms in networked biochemical systems.

The main contributions of this work can be summarized as follows:

- We proposed a generalized enzyme-catalyzed reaction-diffusion model with specific nonlinear forms ($F_1(u, v) = uv$, $F_2(v) = \frac{v}{v+1}$, and $F_3(u) = \gamma u^2$) and systematically analyzed its dynamics on complex network structures.

- Through detailed bifurcation analysis of the homogeneous system, we established the existence conditions for multiple equilibria and identified parameter regions supporting bistability. We rigorously proved the occurrence of subcritical Hopf bifurcation and characterized the stability transitions using Lyapunov coefficient analysis.

- By extending the analysis to network-structured systems, we derived precise conditions for Turing instability, Hopf bifurcation, and Turing-Hopf bifurcation on complex networks. Our theoretical framework explicitly incorporates the network Laplacian eigenvalues, providing a mathematical foundation for understanding topology-dependent pattern formation.

- Numerical simulations on both ER random networks and BA scale-free networks demonstrated that network average degree serves as a crucial control parameter regulating pattern formation. We observed that intermediate connectivity densities favor the emergence of spatiotemporal patterns, while both sparse and dense connectivity tend to suppress pattern formation due to different mechanisms.

- The identification of distinct Turing-Hopf bifurcation points in parameter space revealed the complex interplay between temporal oscillations and spatial patterning, highlighting the rich dynamical repertoire of networked enzyme-catalyzed systems.

Looking forward, our current framework provides a solid foundation for exploring more sophisticated network effects on spatiotemporal pattern formation. Recent studies have begun to investigate the role of higher-order network structures in controlling Turing patterns [18, 22, 23]. These works demonstrate that simplicial complexes and high-order interactions can significantly alter pattern selection and stability. In future research, we plan to extend our enzyme-catalyzed reaction-diffusion model to incorporate such higher-order network topologies, investigating how multi-node interactions and simplicial complexes influence the emergence and stability of spatiotemporal patterns. This direction promises to uncover novel pattern formation mechanisms that cannot be captured by conventional pairwise network models, potentially leading to deeper insights into the organizational principles of complex biochemical systems in structured environments.

***Acknowledgment*:** This work is supported by the Startup Foundation for Introducing Talent of Nanjing Forestry University (Grant No. 163101829).

References

[1] A. M. Turing, The chemical basis of morphogenesis, *Phil. Trans. Roy. Soc. Lond. Ser. B* **237** (1952) 37–72.

[2] Y. Ye, J. Chen, Y. Zhao, Spatiotemporal patterns in a delay-induced infectious disease model with superdiffusion, *Physica D* **476** (2025) #134621.

[3] J. Chen, Y. Ye, Y. Zhao, Fractional diffusion induced pattern formation in an epidemic model with nonlinear incidence rate, *Nonlin. Dyn.* **113** (2025) 31815–31840.

[4] X. P. Yan, J. Y. Chen, C. H. Zhang, Dynamics analysis of a chemical reaction-diffusion model subject to Degen-Harrison reaction scheme, *Nonlin. Anal. Real World Appl.* **48** (2019) 161–181.

[5] R. C. Wu, L. L. Yang, Bogdanov-Takens bifurcation of codimension 3 in the Gierer-Meinhardt model, *Int. J. Bifurc. Chaos* **33** (2023) #2350163.

[6] L. Zhang, C. R. Tian, Turing pattern dynamics in an activator-inhibitor system with superdiffusion, *Phys. Rev. E* **90** (2014) #062915.

[7] B. Fereec, M. Dukaric, O. O. Aybard, I. K. Aybar, Supercritical Hopf bifurcations in two biochemical reaction systems, *MATCH Commun. Math. Comput. Chem.* **85** (2021) 525–544.

[8] J. Su, B. Xu, Local bifurcations of an enzyme-catalyzed reaction system with cubic rate law, *Nonlin. Dyn.* **94** (2018) 521–539.

[9] R. Wu, L. Yang, Bogdanov–Takens bifurcation of an enzyme-catalyzed reaction model, *Nonlin. Dyn.* **112** (2024) 14363–14377.

[10] W. Ko, Bifurcations and asymptotic behavior of positive steady-states of an enzyme-catalyzed reaction-diffusion system, *Nonlinearity* **29** (2016) 3777–3809.

[11] A. Atabaigi, A. Barati, H. Norouzi, Bifurcation analysis of an enzyme-catalyzed reaction-diffusion system, *Comput. Math. Appl.* **75** (2018) 4361–4377.

[12] M. X. Chen, X. Z. Li, Stability analysis and Turing pattern of an enzyme-catalyzed reaction model, *MATCH Commun. Math. Comput. Chem.* **94** (2025) 195–214.

[13] X. Y. Zhao, X. Z. Li, M. X. Chen, Spatiotemporal oscillations of an enzyme-catalyzed model, *MATCH Commun. Math. Comput. Chem.* **94** (2025) 605–631.

[14] M. Chen, X. Li, X.-Z. Li, R. Wu, Turing instability of equilibrium and periodic solution for an enzyme-catalyzed system, *MATCH Commun. Math. Comput. Chem.* **95** (2026) 659–694.

[15] M. E. J. Newman, The structure and function of complex networks, *SIAM Rev.* **45** (2003) 167–256.

[16] J. Zhou, Y. Ye, A. Arenas, S. Gómez, Y. Zhao, Pattern formation and bifurcation analysis of delay induced fractional-order epidemic spreading on networks, *Chaos Solit. Fract.* **174** (2023) #113805.

[17] L. Shi, J. Zhou, Y. Ye, Global stability and Hopf bifurcation of networked respiratory disease model with delay, *Appl. Math. Lett.* **151** (2024) #109000.

[18] Y. Ye, J. Zhou, Y. Zhao, Pattern formation in reaction-diffusion information propagation model on multiplex simplicial complexes, *Inf. Sci.* **689** (2025) #121445.

[19] H. Nakao, A. S. Mikhailov, Turing patterns in network-organized activator–inhibitor systems, *Nat. Phys.* **6** (2010) 544–550.

[20] P. Erdős, A. Rényi, On the evolution of random graphs, *Publ. Math. Inst. Hung. Acad. Sci.* **5** (1960) 17–60.

[21] A. L. Barabási, R. Albert, Emergence of scaling in random networks, *Science* **286** (1999) 509–512.

[22] R. Muolo, L. Gallo, V. Latora, M. Frasca, T. Carletti, Turing patterns in systems with high-order interactions, *Chaos Solit. Fract.* **166** (2023) #112912.

[23] S. Gao, L. Chang, M. Perc, Z. Wang, Turing patterns in simplicial complexes, *Phys. Rev. E* **107** (2023) #014216.